Theoretical and Applied Mechanics Letters 15 (2025) 100617

Contents lists available at ScienceDirect

Theoretical and Applied Mechanics Letters

journal homepage: www.elsevier.com/locate/taml

Research Article

Numerical simulation study of hypersonic MHD control at mid–low altitudes ☆

Yongchun Yan [a,b,c,d], Juan Ma [a,c,d,*], Mingsong Ding [b], Jianqiang Chen [b,*]

[a] Joint Laboratory of International Cooperation on Structural Mechanics of Composite Materials for Electronic Devices, Xi'an 710071, China
[b] State Key Laboratory of Aerodynamics, Mianyang 621000, China
[c] School of Information Mechanics and Sensing Engineering, Xidian University, Xi'an 710071, China
[d] Research Center of Applied Mechanics, School of Electro-Mechanical Engineering, Xidian University, Xi'an 710071, China

ARTICLE INFO

Keywords:
Magnetohydrodynamic (MHD)
Hypersonic
Mid-low altitude
Thermal protection
Numerical simulation

ABSTRACT

Hypersonic magnetohydrodynamic (MHD) control effectively enhances the aerothermal environment of aerospace vehicles, demonstrating considerable potential in plasma flow regulation and aerodynamic optimization. As aerospace vehicles progress toward mid-low-altitude hypersonic regimes, their external aerothermal conditions become increasingly severe. This study addresses the challenges of complex aerodynamic force/heat environments and the difficulties in MHD control numerical simulations for hypersonic vehicles at mid-low altitudes. On the basis of the perfect gas model and the low magnetic Reynolds number assumption, we conduct numerical simulations of MHD control under mid-low altitudes, high-Mach-number conditions. The findings reveal the following: (1) the low magnetic Reynolds number assumption is valid and computationally accurate, as corroborated by a comparative analysis with the literature; (2) in the mid-low altitude hypersonic regime, magnetic fields significantly suppress the shock standoff distance and reduce the surface heat flux. Both the magnetically controlled shock wave and the thermal protection exhibit nonlinear variations with the Mach number, increasing and then decreasing as the Mach number increases. The optimal Mach number for shock wave control is 13, whereas optimal thermal protection is achieved at Mach 15. At an altitude of 40 km, the optimal magnetohydrodynamic Mach range spans 13–17, achieving a maximum heat flux attenuation of 28.81 %. Additionally, the effects of magnetic shock wave control correlate approximately exponentially with altitude within certain parameters, whereas the efficacy of thermal protection behaves linearly with altitude variations.

1. Introduction

With the continuous advancement of hypersonic flight technology, there has been a surge of interest and enthusiasm in the research of hypersonic vehicles. However, increasing flight velocities have introduced new challenges regarding the structural design and material selection of these vehicles. Since the 1990s, magnetohydrodynamic (MHD) has emerged as a prominent field in hypersonic applications. By introducing momentum and energy into hypersonic flow fields through magnetic field generation systems, researchers have been able to effectively control and optimize aerodynamic environments and performance. Compared with traditional mechanical control methods, this approach offers advantages such as simplified structural design and reduced added mass [1], attracting significant global attention. In China, MHD and plasma dynamics have been designated critical components of "Significant Aerodynamic Mechanics Issues in Aerospace" within the national strategic research category of the National Medium- and Long-Term Scientific and Technological Development Plan (2006–2020) [2].

Magnetic thermal protection technology, a critical area of research within MHD control, employs Lorentz forces produced by applied magnetic fields to deflect shock waves away from vehicle surfaces. This mechanism reduces the fluid velocity and decreases the temperature gradient within the boundary layer, thereby effectively diminishing the wall heat flux and simplifying the complexity of the thermal protection design [3]. In recent years, rapid advancements in MHD control technologies and computational capabilities have ushered in a new era of development for numerical simulations of hypersonic vehicle MHD control systems.

The electrical conductivity of plasma in the external flow field of hypersonic vehicles is generally low. Therefore, the "low magnetic Reynolds number assumption" is often adopted in numerical simulations of hypersonic external flow fields. By employing low magnetic Reynolds

---

☆ This document is the results of the research project funded by National Numerical Wind Tunnel Project of China.

* Corresponding authors.
E-mail addresses: jma@xidian.edu.cn (J. Ma), chenjq@cardc.cn (J. Chen).

https://doi.org/10.1016/j.taml.2025.100617
Received 26 April 2025; Received in revised form 7 September 2025; Accepted 8 September 2025

number MHD equations, this approach effectively avoids numerical singularities and stiffness issues, reduces unnecessary computational complexity, and enhances both stability and efficiency in simulations. For example, in 2016, Li et al. [4] utilized a low magnetic Reynolds number MHD model to analyze the feasibility of conventional solenoids in numerical simulations of hypersonic nose-cone flow fields. In 2017, Wang et al. [5], on the basis of the low magnetic Reynolds number assumption, investigated the influence of key parameters—such as the position and width of surface MHD acceleration/deceleration actuation, magnetic field strength, electrical conductivity, and energy conversion efficiency—on wedge shock waves. In 2018, Yao et al. [6] employed the low magnetic Reynolds number MHD model to study the effects of different magnetic field configurations on flow field structures, aerodynamic drag, and Lorentz forces, along with their underlying mechanisms. In 2019, Ding et al. [7] addressed the accuracy of conductivity modeling and its impact on hypersonic MHD control. Using the low magnetic Reynolds number method, they analyzed how conductivity simulations affect hypersonic MHD flow field distributions and aerodynamic force/heat characteristics. In 2020, Ding et al. [8], still under the low magnetic Reynolds number assumption, examined the influence of different gas models on hypersonic MHD control simulations. In 2021, Luo et al. [9] explored the mechanisms and patterns of how varying magnetic induction intensities and magnet placements affect the flow structures and key parameter distributions around a double-cone model.

With the expansion of flight altitude, velocity, and magnetic field parameters, hypersonic MHD control technologies face increasing challenges in extreme environments and propulsion conditions, including thermal reduction, drag minimization, and control system optimization. Since 2007, the European Space Agency has funded experimental studies on magnetic thermal protection conducted by the German Aerospace Center and CIRA [10]. For example, Gulhan et al. [11] demonstrated in wind tunnel experiments that the application of magnetic fields reduced heat flux by 46 % and 85 % for hemispherical and flat-face cylindrical configurations, respectively. The Bisek team at the U.S. Air Force Research Laboratory [12] conducted MHD numerical simulations of a blunt-nosed elliptical cone with vertical stabilizers under the low magnetic Reynolds assumption, analyzing the magnetic effects on leading-edge heat flux. However, because of the low local electrical conductivity ($\sigma < 0.1$ S·m^{-1}) at the leading edge, magnetic thermal protection remained negligible. Bityurin and Bocharov from Russia's High-Temperature Institute [13] employed a perfect gas model and dipole magnetic configurations to numerically simulate magnetic thermal protection for simplified reentry capsule geometries, thereby revealing effective stagnation-point heat flux reduction via magnetic field optimization. Li Kai and Liu Jun from the National University of Defense Technology [14], using the low magnetic Reynolds number assumption, investigated magnetic thermal protection system modeling for simple blunt-body configurations. Their studies showed that increasing the solenoid radius enhances the thermal protection efficacy, whereas variations in the solenoid length yield relatively minor effects. Ding Mingsong from the China Aerodynamics Research and Development Center [15] and colleagues performed simulation studies on magnetic thermal protection systems for high-speed "glide-return" spaceplane configurations resembling NASA's Space Shuttle Columbia (OV-102). By evaluating five magnetic field configurations across different flow parameters (Mach number and altitude), they demonstrated that optimized magnetic setups effectively reduce the surface heat flux and improve the thermal environment. Additionally, Teng Ziang's team at Beihang University [16] numerically simulated MHD thermal protection flow control, revealing a 20 % reduction in stagnation-point heat flux density at an altitude of 50 km and Mach numbers of 16–18. At an altitude of 60 km, the efficacy of magnetic thermal protection increases with altitude, achieving a 42.10 % reduction in stagnation-point heat flux density.

In summary, although extensive research has been conducted globally on hypersonic MHD control, with the low magnetic Reynolds number method and its flow control efficacy being widely acknowledged and validated, most studies have concentrated on high-altitude conditions; relatively few investigations have addressed MHD control in medium- to low-altitude hypersonic regimes. The aerothermal environment at medium-low altitudes is particularly severe, and numerical simulations under such conditions present significant challenges.

The authors conducted extensive investigations into hypersonic flow numerical simulations, establishing a solid research foundation. On the basis of the self-developed aerophysical computational platform (AEROPH), this study introduces fundamental MHD control theories and models to construct a hypersonic MHD flow control model. The stability and accuracy of the associated numerical scheme have been rigorously validated. To build upon this framework, numerical simulations of MHD flow control under mid-to-low altitude and high-Mach-number conditions were performed. The objective is to investigate the influence of key parameters—such as the flight altitude and freestream Mach number—on shock wave modulation and thermal protection characteristics in hypersonic vehicles via magnetic control.

2. Physical model and numerical methodology

2.1. Governing equations and solution framework

In hypersonic flow fields around aerospace vehicles, the plasma present in external flow regions typically exhibits low-electrical conductivity characteristics, which satisfy the low magnetic Reynolds number assumption ($Re_m << 1$) [17]. Under such conditions, the induced magnetic field is negligible in comparison to the externally applied magnetic field. Consequently, the dimensionless governing equations that incorporate electromagnetic effects can be formulated as follows [18]:

$$\frac{\partial \mathbf{Q}}{\partial t} + \frac{\partial \mathbf{F}}{\partial x} + \frac{\partial \mathbf{G}}{\partial y} + \frac{\partial \mathbf{H}}{\partial z} = \frac{1}{Re}\left(\frac{\partial \mathbf{F_V}}{\partial x} + \frac{\partial \mathbf{G_V}}{\partial y} + \frac{\partial \mathbf{H_V}}{\partial z}\right) + \mathbf{W} + \mathbf{W}_{\mathrm{MHD}}, \tag{1}$$

where x, y, and z represent the three orthogonal spatial coordinates in a Cartesian coordinate system; Re denotes the Reynolds number. Here

$$\mathbf{Q} = \begin{bmatrix}\rho & \rho u & \rho v & \rho w & \rho U\end{bmatrix}^{\mathrm{T}}, \tag{2}$$

where ρ represents the mixture density; u, v, and w represent the velocity components in the x, y, and z directions of the Cartesian coordinate system, respectively; U signifies the total energy; $\mathbf{F}$, $\mathbf{G}$, and $\mathbf{H}$, and $\mathbf{F}_V$, $\mathbf{G}_V$, and $\mathbf{H}_V$ are the inviscid fluxes and viscous fluxes in the three Cartesian coordinate directions x, y, and z, respectively; $\mathbf{W}$ denotes the source term for perfect gas equilibrium, whose value is zero. The variable $\mathbf{W}_{\mathrm{MHD}}$ is the electromagnetic source term, which can be expressed as

$$\mathbf{W}_{\mathrm{MHD}} = Q_m \cdot \left[\sigma\,(\mathbf{J}\times \boldsymbol{B})_x \; (\mathbf{J}\times \mathbf{B})_y \; (\mathbf{J}\times \mathbf{B})_z \; \mathbf{J}\cdot\mathbf{E}\right]^{\mathrm{T}}, \tag{3}$$

where σ is the electrical conductivity of the gas mixture; $\mathbf{J}$ represents the current density; $\mathbf{B}$ denotes the magnetic induction field; $\mathbf{E}$ represents the electric field; $(\mathbf{J}\times\mathbf{B})_x$ signifies the Lorentz force contribution to momentum transport in the x direction. The magnetic interaction parameter (Q_m) quantifies the overall coupling efficiency between the magnetic field and the flow field, representing their synergistic interaction effects

$$Q_m = \frac{\sigma_0 B_0^2 L}{\rho_0 u_0}, \tag{4}$$

where σ_0, B_0, L, ρ_0, and u_0 represent the electrical conductivity, magnetic induction strength, characteristic length scale of the region influenced by the magnetic field, fluid density, and characteristic flow velocity, respectively.

The inviscid terms in Eq. (1) are discretized via the AUSMPW+ (advection upstream splitting method with pressure-based weighting functions) scheme to balance computational accuracy and efficiency. Viscous terms employ central differencing, whereas temporal integration employs an LU-SGS (lower-upper symmetric Gauss–Seidel) implicit

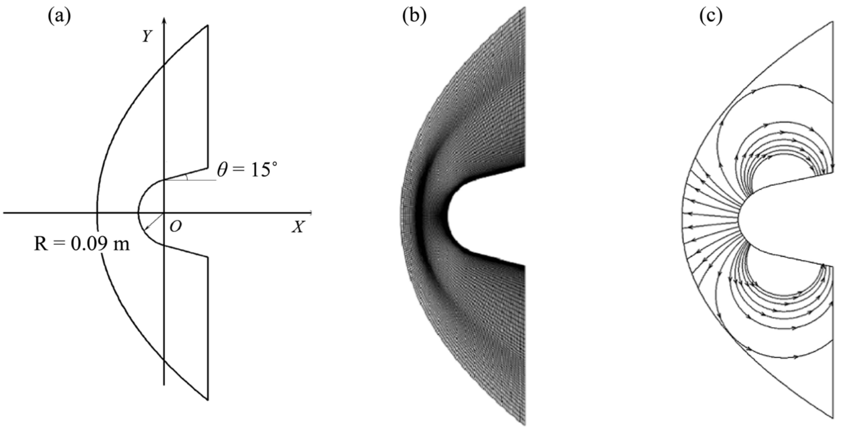

Fig. 1. Blunt cone model and computational domain. (a) Structural schematic diagram. (b) Mesh distribution diagram. (c) Magnetic field line distribution diagram.

method. Insulating boundary conditions are applied to walls, inlets and outlets because of their low electrical conductivity, thereby enforcing nonpenetrating current conditions ($\mathbf{J} \cdot \mathbf{n} = 0$).

2.2. Electrodynamics model

Under the low magnetic Reynolds number condition for weakly ionized gases, the influence of the induced magnetic field can be neglected. If a steady (quasi-steady) magnetic field is applied, then $\partial \mathbf{B}/\partial t = 0$. Combining this equation with Faraday's law of electromagnetic induction yields:

$$\nabla \times \mathbf{E} = -\frac{\partial \mathbf{B}}{\partial t} = \mathbf{0}. \tag{5}$$

In a converged steady (or quasi-steady) state, the electric field is irrotational. Consequently, this field can be expressed as the gradient of a scalar potential function as follows:

$$\mathbf{E} = -\nabla \phi. \tag{6}$$

In hypersonic plasma, the plasma constituents approximately satisfy the principle of quasineutrality, whereas the current density conforms to the continuity equation as follows:

$$\nabla \cdot \mathbf{J} = 0, \tag{7}$$

where $\mathbf{J}$ is determined by the generalized Ohm's law, which states:

$$\mathbf{J} = \tilde{\sigma}(\mathbf{E} + \mathbf{V} \times \mathbf{B}). \tag{8}$$

In these equations, $\tilde{\boldsymbol{\sigma}}$ represents the electrical conductivity tensor, and $\mathbf{V}$ is the flow velocity.

In the context of hypersonic plasma flows, the Hall and ion slip effects are typically regarded as negligible. This consideration simplifies the generalized Ohm's law as follows:

$$\mathbf{J} = \sigma(\mathbf{E} + \mathbf{V} \times \mathbf{B}). \tag{9}$$

Substituting into Eq. (5) and simplifying yields:

$$\nabla \cdot (\sigma \nabla \boldsymbol{\phi}) = \nabla \cdot [\sigma(\mathbf{V} \times \mathbf{B})]. \tag{10}$$

By coupling Eq. (1), the electric potential function $\boldsymbol{\phi}$, and electric field $\mathbf{E}$, are initially obtained by numerically solving Eq. (10). The current density, $\mathbf{J}$, is subsequently derived via Eq. (9), which ultimately determines the source terms of the governing flow equations.

2.3. Conductivity model

In hypersonic external flow fields, the electrical conductivity is commonly recognized to remain relatively low. In weakly ionized plasma states, conductivity is not only influenced by thermodynamic parameters such as temperature and pressure but also closely correlated with the degree of ionization. Macheret and Shneider [19] demonstrated that under low ionization conditions ($X_e = 10^{-2} - -10^{-3}$), the electrical conductivity σ is approximately proportional to the ionization fraction X_e. Therefore, this study employs the conductivity model proposed by the Macheret model as follows:

$$\sigma = 2.7 \times 10^5 X_e X_e \le 10^{-2} - -10^{-3}. \tag{11}$$

Here, the electron mole fraction is treated via the methodology described in Reference [20], where the flow is approximated to reach thermodynamic and chemical equilibrium under these conditions. On the basis of the ideal MHD assumption, the electron mole fraction within the flow field is calculated via the following fitted formula:

$$X_e = \begin{cases} \varepsilon + X_0 \cdot \mathrm{th}\left[\left(T - T_0\right)/D\right], T \ge T_0, \\ 0, \quad T < T_0, \end{cases} \tag{12}$$

where th is the hyperbolic tangent function, $\varepsilon = 10^9$, $T_0 = 3000$ K, $D = 3000$ K, and $X_0 = 0.002$.

3. Validation of representative test cases

A blunt cone configuration is employed as the test case, with its computational domain structure and mesh illustrated in Fig. 1(a) and (b). The model features a nose radius of $R = 0.09$ m, a half-angle of 15°, and a total length of $L = 0.1224$ m. The mesh density adheres to the specifications outlined in Reference [21]. The simulation parameters include a flight altitude of $H = 40$ km, a freestream temperature of $T = 250.35$ K, a Mach number of $Ma_\infty = 15$, and a wall temperature of $T_w = 800$ K. As shown in Fig. 1(c), an applied magnetic dipole field is configured to simulate the magnetic environment produced by practical solenoid coils as

$$\mathbf{B} = B_0 \left[\frac{\cos\theta}{\left(r/r_0\right)^3} \mathbf{r} + \frac{\sin\theta}{2\left(r/r_0\right)^3} \boldsymbol{\theta} \right], \tag{13}$$

where $(\mathbf{r}, \boldsymbol{\theta})$ denotes the unit vectors in polar coordinates; r and θ represent the corresponding scalar quantities; the dipole center is located at the origin of the coordinate system, i.e., the center of the blunt cone; and B_0 is the magnetic induction strength along the polar axis at a distance r_0 from the dipole center. Here, $B_0 = 2.0$ T and $r_0 = 0.09$ m.

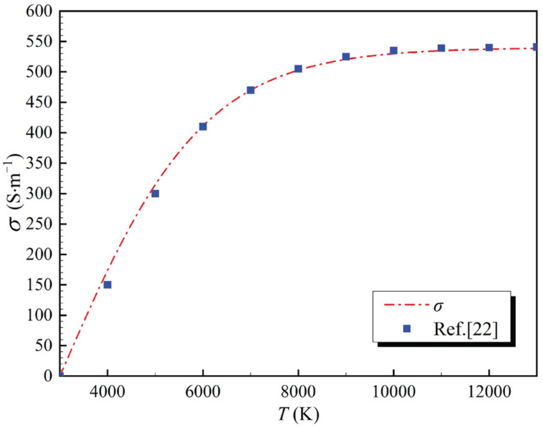

Fig. 2. Electrical conductivity comparison with the literature [22].

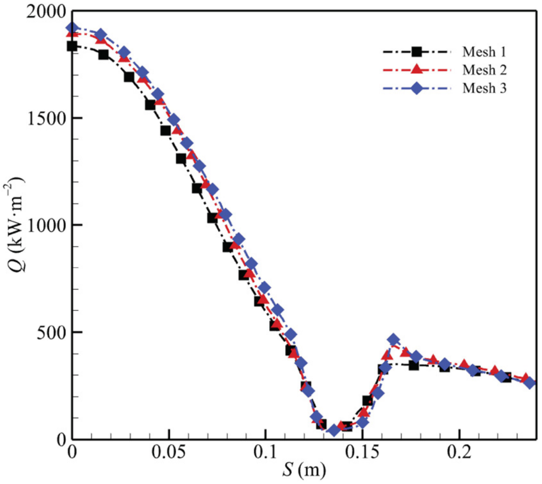

Fig. 3. Grid independence test for Mesh 1, Mesh 2, and Mesh 3.

3.1. Validation of the electrical conductivity model

The variation in electrical conductivity with temperature is shown in Fig. 2, and the computed results are in excellent agreement with those reported in [22], thereby validating the reliability of the adopted conductivity model.

3.2. Validation of the numerical method

A mesh independence test was initially conducted, and the results are presented in Fig. 3, where Mesh1 (coarse grid) consists of 61 × 91 nodes; Mesh2 (medium grid) comprises 81 × 121 nodes; and Mesh3 (fine grid) contains 121 × 181 nodes.

As indicated in Fig. 3, excellent mesh independence is achieved, with the results from Mesh2 and Mesh3 demonstrating nearly identical agreement. Considering both computational accuracy and efficiency, Mesh2 is selected for the study.

Figure 4 presents a comparison of the surface heat flux density distributions between the present blunt cone case and the results from Reference [23]. Here, S denotes the arc length along the surface of the blunt cone, and Q represents the surface heat flux density. The computed values of heat flux density in this study align closely with those reported in Reference [23], demonstrating excellent numerical consistency.

Figure 5 illustrates the convergence behavior of the normalized residuals for the simulated case. The results demonstrate that the solution achieves satisfactory convergence after approximately 8000–10000 iterations, with the residual norms dropping below 10^{-5}.

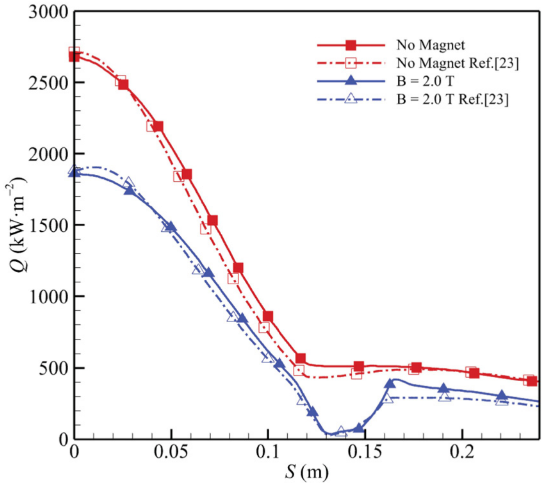

Fig. 4. Comparison of the surface heat flux density with that in the literature [23].

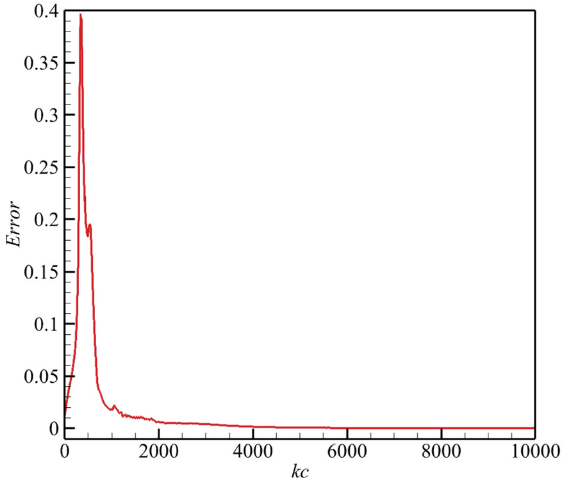

Fig. 5. Convergence history of residuals.

3.3. Parametric sensitivity analysis

Figure 6 presents the parametric sensitivity analysis results for the Mach number and flight altitude. As shown in Fig. 6(a), when the Mach number varies within ±0.1, the surface heat flux exhibits an overall increasing trend with increasing Mach number, which agrees well with the theoretical predictions. Similarly, Fig. 6(b) shows that $a \pm 1$ km variation in flight altitude leads to a decreasing trend in surface heat flux with increasing altitude, which is consistent with the results of theoretical calculations. These results confirm that the developed MHD control model maintains good accuracy and stability. Furthermore, the observed Mach number and flight altitude dependencies highlight their critical role in determining the effectiveness of MHD-based thermal protection systems.

4. MHD numerical simulation

4.1. Parameter setting and numerical simulation

This study maintains the same configuration as outlined in Section 3, with flight altitudes of H = 20–40 km, Mach numbers of Ma = 5–20, and magnetic induction strengths of B = 0.0 T and 2.0 T. The parameter settings are provided in Table 1.

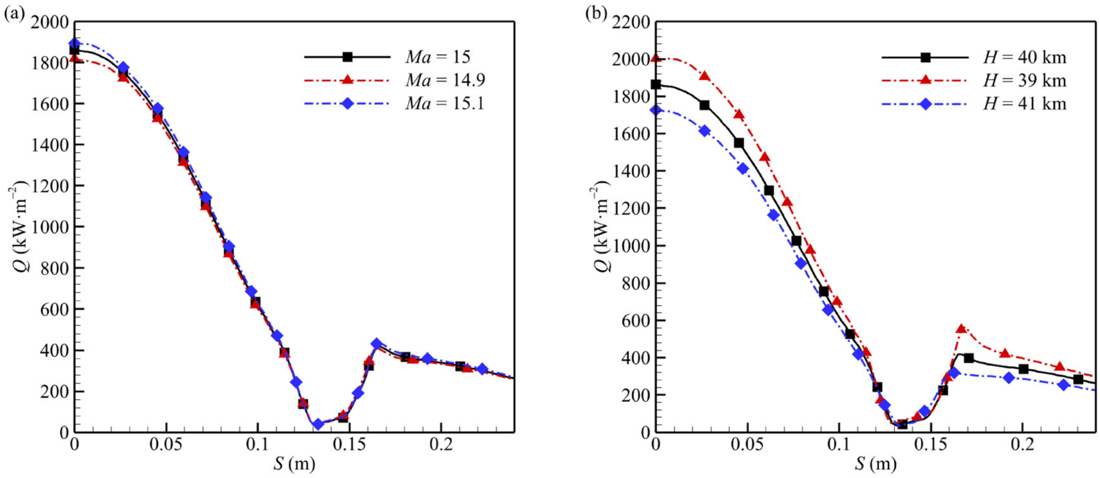

Fig. 6. Parametric sensitivity analysis. (a) Mach. (b) Flight altitude.

Table 1
Parameter configuration for blunt cone simulation cases.

Flight altitude (km)	Free-stream Mach number Ma	Free-stream temperature (K)	Free-stream pressure (Pa)	Magnetic induction (T)
40	5, 7, 9, 11, 13, 15, 20	250.35	287.144	0.0 2.0
35		236.513	574.595	0.0 2.0
30		226.509	1197.03	0.0 2.0
25		221.552	2549.22	0.0 2.0
20		216.65	5529.31	0.0 2.0

The applied magnetic field is generated by a solenoid coil, adhering to the dipole distribution scheme described in Section 3. The solenoid parameters are set as follows: $B_0 = 2.0$ T and $r_0 = 0.09$ m. The direction of the magnetic field aligns with the positive x-axis of the coordinate system, with its center coincident with the origin.

4.2. Study of Mach number effects

Using a flight altitude of H = 40 km as an example, the effects of Mach numbers ranging from 5–20 on the magnetically controlled shock wave and thermal protection performance of the blunt cone configuration, along with an analysis of the underlying mechanisms, are investigated in this section.

Figure 7 illustrates the influence of magnetic fields on flow-field structures at different Mach numbers, using the temperature field as an example. The abrupt temperature gradient regions indicate shock wave locations. When $Ma = 7$, the magnetic field has a negligible effect on the external flow field structure of the blunt cone. However, when $Ma \geq 9$, the magnetic field significantly alters the flow field structure. As the Mach number increases, the temperature distribution becomes more pronounced, and the shock standoff distance—the separation between the shock wave and the vehicle surface—also increases notably.

A comparison of Fig. 7(a) and (d) reveals that the shock standoff distance reaches a maximum value within this Mach number interval. According to MHD control mechanisms, this distance is influenced not only by the parameters of the magnetic field but also directly by the electrical conductivity of the air in the magnetically controlled region [3]. Under conditions of a constant magnetic field, the magnitude of post-shock electrical conductivity directly determines the strength of the counterflow Lorentz force, thereby playing a decisive role in the shock standoff distance within this specific Mach number range.

The variation in electrical conductivity at a post-shock point ($x = -0.1$ m) as a function of the Mach number is presented in Fig. 8(a). For Mach numbers below 7, the post-shock conductivity remains at approximately 10^{-2} S·m^{-1}, indicating negligible ionization within the shock region. When Ma =7–11, the rate of increase in conductivity progressively accelerates as ionization intensifies within the shock layer. When Ma >11, although the conductivity continues to rise, its growth rate gradually decreases; however, the spatial extent of ionization expands continuously.

The contour plot of the electrical conductivity distribution at Mach number 13 is presented in Fig. 8(b). Outside the shock wave, the gas exhibits extremely low conductivity, indicating negligible ionization. Within the shock layer, ionization is substantial, with conductivity decreasing gradually in the downstream flow direction. The highest conductivity values are observed near the blunt cone nose region. When considered alongside Figs. 7 and 8, this finding indicates that as the Mach number increases, the gas temperature within the shock layer progressively increases, the ionization degree of the gas intensifies concomitantly, and the spatial extent of the post-shock ionized region expands correspondingly.

Figure 9 presents the variation in the magnetic interaction parameter, Q_{m}, with the Mach number. The Q_m effectively quantifies the overall coupling efficiency between the magnetic field and the flow field [3]. As indicated by Eq. (4), Q_m is directly proportional to the electrical conductivity and the square of the magnetic induction strength and inversely proportional to the fluid density and freestream velocity.

Figure 10 presents the variation in the shock standoff distance with the Mach number. Specifically, Fig. 10(a) compares the shock standoff distances with and without magnetic field effects, whereas Fig. 10(b) illustrates the shock extrapolation distance (quantifying the influence of the magnetic field on the shock standoff distance).

From Figs. 9 and 10, the following observations can be made:

(1) Without a magnetic field: in the absence of a magnetic field, Q_m remains zero at all Mach numbers. The shock standoff distance gradually decreases as the Mach number increases, asymptotically approaching a fixed value, in accordance with the Mach number independence principle.

(2) With a magnetic field, when $Ma < 7$, post-shock gas ionization remains negligible, resulting in an extremely low Q_m. The magnetic field has no appreciable influence on the shock standoff distance. When Ma = 7–11, as the Mach number increases, post-shock gas ionization intensifies due to rising temperatures, thereby expanding the ionized region. The counterflow Lorentz force and Q_m rapidly in-

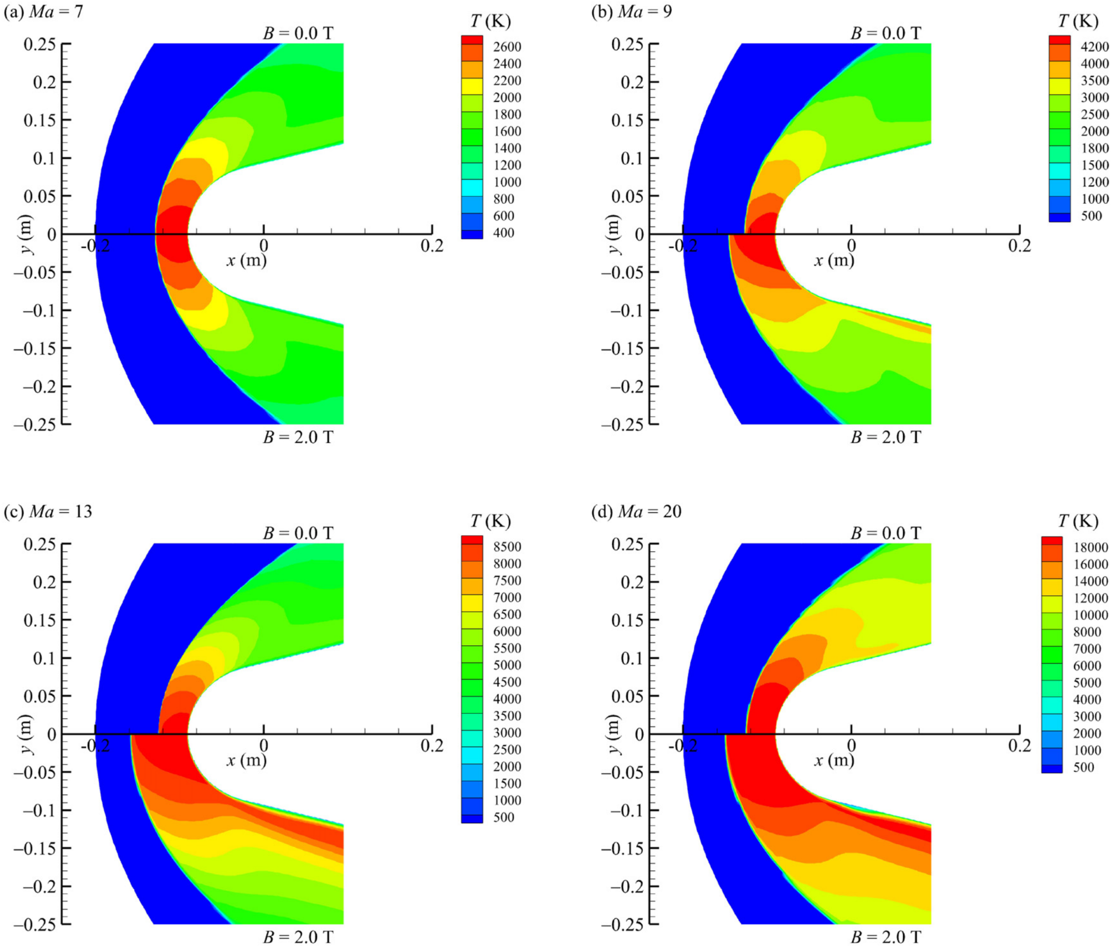

Fig. 7. Influence of the magnetic field on the flow-field structure at *Ma*=5–20. (a) *Ma*=7. (b) *Ma*=9. (c) *Ma*=13. (d) *Ma*=20.

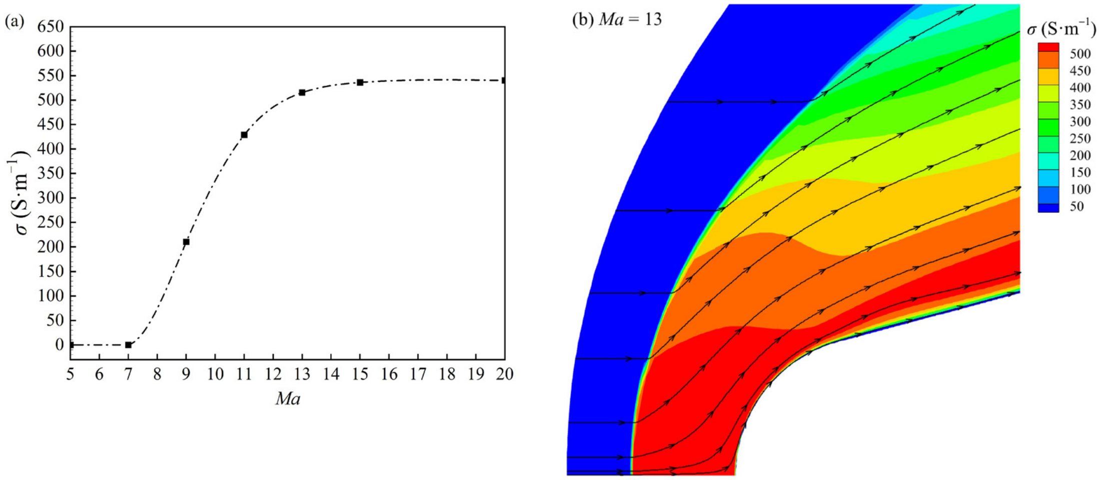

Fig. 8. Variation in the electrical conductivity distribution. (a) Variation of post-shock electrical conductivity with Mach number. (b) Electrical conductivity contour at *Ma* = 13.

crease. The Lorentz force becomes a dominant factor in shock wave displacement, significantly enhancing the rate of shock extrapolation. Beyond Mach 13, as the Mach number continues to increase, the spatial extent of post-shock ionization gradually decreases, the incremental growth of the counterflow Lorentz force diminishes, and Q_m gradually decreases. Consequently, the shock standoff distance also decreases slightly.

The maximum distance of shock standoff is attained within the Mach number range of 11–13.

Previous studies [10–16,24] have demonstrated that magnetic thermal protection can effectively reduce surface heat flux in aerospace vehicles. The magnetically controlled thermal protection performance of the blunt cone configuration was further investigated in this study. The variation in the surface heat flux density on the blunt cone under differ-

Table 2
Stagnation-point heat flux density and reduction percentage for the blunt cone.

Mach number		5	7	9	11	13	15	20
Stagnation-point heat flux density (kW·m^{-1})	B = 0.0 T	53.6	211.5	532.4	948.5	1777.9	2678.7	5173.6
	B = 2.0 T	53.6	211.5	474.6	757.6	1307.5	1907.0	4499
Reduction Percentage (%)		0	0	10.86	20.13	26.46	28.81	13.04

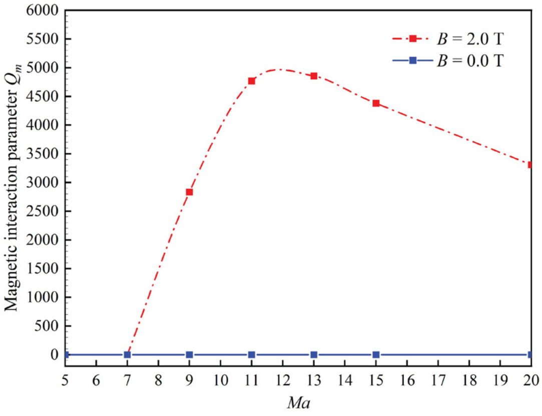

Fig. 9. Variation in Q_m with the Mach number.

ent Mach number conditions is shown in Fig. 11. As the Mach number increases, both the heat flux density with and without a magnetic field exhibit an overall increasing trend. For Mach numbers between 5 and 7, the magnetic field has minimal influence on the surface heat flux density. However, when $Ma > 7$, the magnetic field significantly impacts the surface heat flux density, with the disparity between the magnetic and nonmagnetic cases becoming increasingly pronounced as the measurement location approaches the stagnation point.

The thermal environment in the nose region of the vehicle is the most severe. The focus of this study is to investigate the effects of magnetic thermal protection in the nose area ($S = 0$ m). The stagnation-point heat flux density values and their reductions under various operating conditions are presented in Table 2.

From Table 2 and Fig. 9, the following observations can be made:

When $Ma < 7$, the post-shock conductivity remains at approximately 10^{-2} S·m^{-1}, resulting in an extremely low Q_m. The counterflow Lorentz force has a negligible influence on the boundary layer, and the magnetic field has a minimal effect on the stagnation-point heat flux.

When Ma = 7–15, as the post-shock conductivity increases, Q_m also increases progressively. The influence of the counterflow Lorentz force on the boundary layer becomes stronger, resulting in a significant increase in the magnetic field's ability to reduce heat flux. Consequently, the stagnation-point heat flux reduction also increases.

Beyond Mach 15, as the Mach number continues to increase, the post-shock conductivity stabilizes, Q_m gradually decreases, and the effect of the counterflow Lorentz force on the boundary layer diminishes. Consequently, the efficacy of the magnetic field in mitigating heat flux weakens, and the rate of the reduction in the stagnation-point heat flux decreases.

A maximum heat flux reduction of 28.81 % is achieved at Ma = 15. On the basis of the data presented in Table 2, the surface heat flux reduction curve was fitted and is illustrated in Fig. 10.

When the reduction in stagnation-point heat flux exceeds 25 %, the effectiveness of magnetic thermal protection becomes significant. As shown in Fig. 12, for the blunt cone configuration with a magnetic induction strength of 2.0 T, the optimal range for the magnetic control Mach number is 13–17. Within this range, the shock standoff distance spans a range of 61–66 mm, and the maximum reduction in stagnation-point heat flux reaches 26.46 %–28.81 %.

4.3. *Study of the influence of flight altitude*

The variations in the magnetic interaction parameter and shock standoff distance with the Mach number at different flight altitudes are shown in Figs. 13 and 14. As the flight altitude increases, the air density decreases significantly, resulting in a marked increase in Q_m. For all the flight altitudes studied, Q_m initially increases with the Mach number before subsequently decreasing, reaching its maximum value at Mach 11–13. This trend is consistent across all altitude conditions.

As demonstrated in Figs. 13 and 14(a), when $Ma < 7$, the magnetic field has no appreciable influence on the shock standoff distance. When $Ma > 7$, the flight altitude has a minimal effect on the Mach number-dependent variation in the shock standoff distance, which consistently shows an initial rapid increase followed by a gradual decline across all altitudes. The maximum shock standoff distance occurs at Ma = 11–13, irrespective of the flight altitude.

The underlying physical mechanisms that govern this behavior were detailed in earlier sections and will not be reiterated here.

As shown in Fig. 14(b), the flight altitude does not affect the variation pattern of the shock extrapolation distance. The displacement consistently tends to initially increase and then decrease as the Mach num-

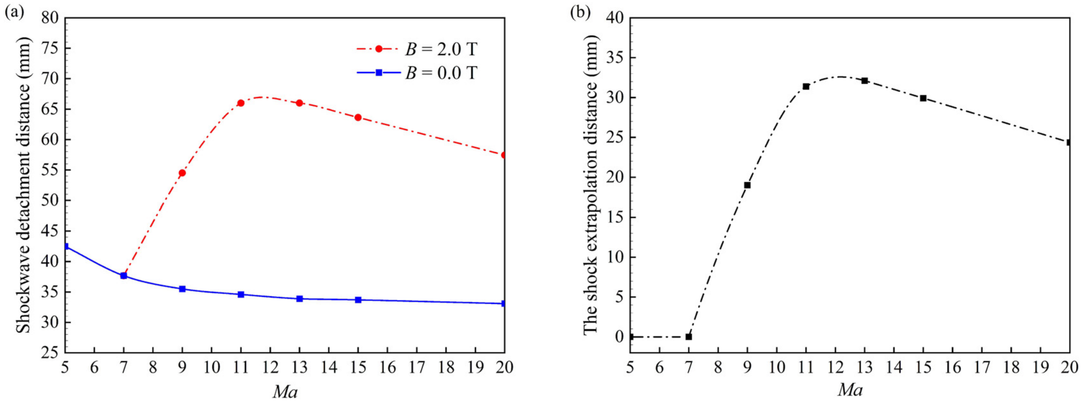

Fig. 10. Mach number dependence of the shock standoff distance. (a) With and without magnetic field. (b) The shock extrapolation distance.

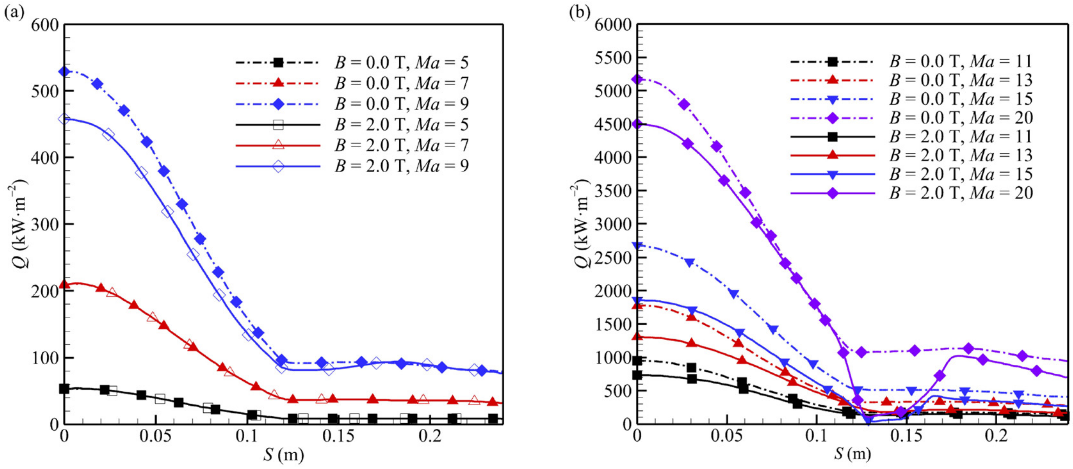

Fig. 11. Variations in the surface heat flux density with the Mach number (with and without a magnetic field). (a) Ma = 5–9. (b) Ma = 11–20.

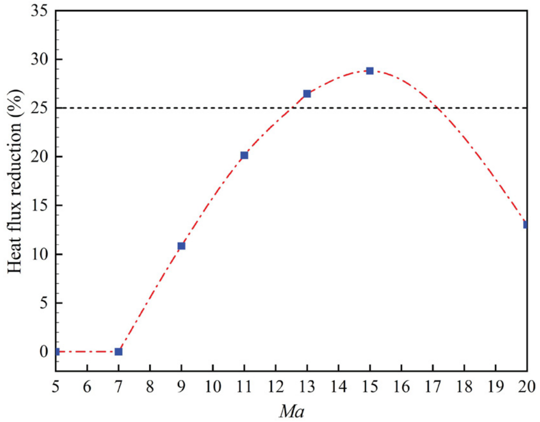

Fig. 12. Variation in stagnation-point heat flux reduction with Mach number.

ber increases, with the maximum shock extrapolation distance occurring at Mach 13 across all altitudes. As the flight altitude decreases, the magnetic interaction parameter diminishes, thereby weakening the influence of the counterflow Lorentz force on shock wave control. Consequently, the shock extrapolation distance is significantly reduced, and the MHD shock control effect progressively deteriorates.

The percentages of stagnation-point heat flux reduction and the corresponding variation curves for the blunt cone configuration at different flight altitudes (H = 20–40 km) are presented in Table 3 and Fig. 15.

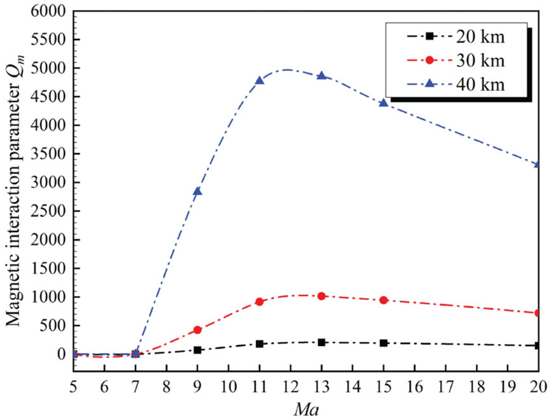

Fig. 13. Variation in Q_m with the Mach number at flight altitudes (H = 20–40 km).

Table 3
Stagnation-point heat flux reduction at different flight altitudes.

Mach number		5	7	9	11	13	15	20
Reduction percentage (%)	20 km	0	0	0	0.49	1.31	4.56	3.38
	30 km	0	0	4.01	5.28	8.73	18.41	6.89
	40 km	0	0	10.86	20.13	26.46	28.81	13.04

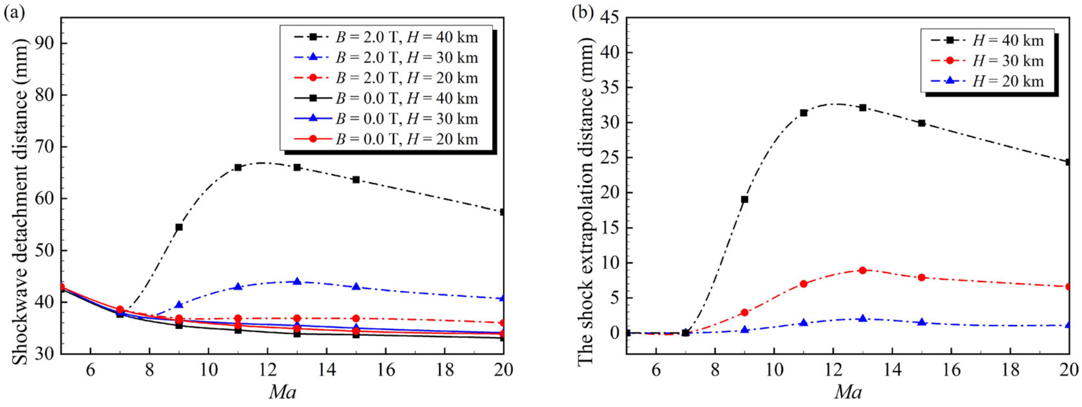

Fig. 14. Mach number dependence of the shock standoff distance. (a) With and without magnetic field. (b) The shock extrapolation distance.

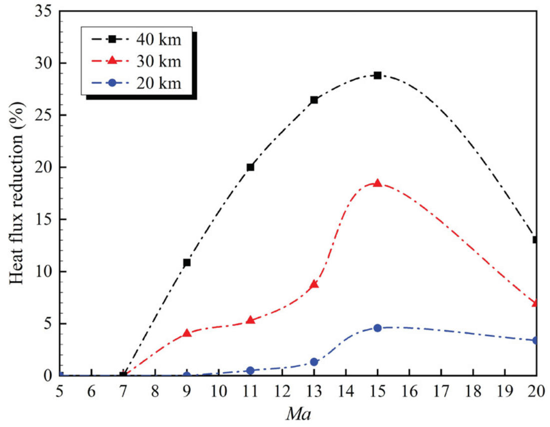

Fig. 15. Variation in stagnation-point heat flux reduction at flight altitude ($H = 20$–40 km).

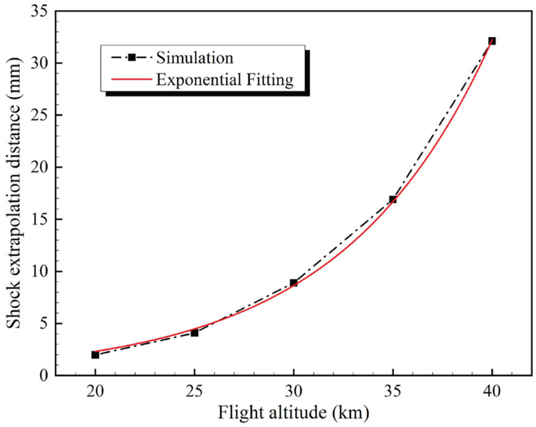

Fig. 16. Curve of the shock extrapolation distance at $Ma = 13$.

As shown in Fig. 15, when $Ma < 7$, the flight altitude has no discernible effect on the reduction in stagnation-point heat flux. When $Ma > 7$, the influence of the flight altitude on the variation in stagnation-point heat flux reduction with the Mach number remains marginal. Across all the flight altitudes, the heat flux reduction initially tends to increase but then decreases, with the maximum reduction occurring universally at $Ma = 15$.

As the flight altitude decreases, Q_m significantly decreases. This leads to a gradual weakening of the influence of the counterflow Lorentz force on the boundary layer, thereby causing a substantial decline in the efficacy of magnetic thermal protection.

In summary, at varying flight altitudes, the maximum shock extrapolation distance occurs at $Ma = 13$, whereas the maximum reduction in surface heat flux is achieved at $Ma = 15$. The variations in these maximum shock extrapolation distance values and surface heat flux reductions as the flight altitude increases are illustrated in Figs. 16 and 17.

As shown in Fig. 16, the shock extrapolation distance exhibits an exponential increase with increasing flight altitude, adhering to the following exponential fitting formula:

$$y = ae^{bx}, \tag{14}$$

where $a = 0.178$ and $b = 0.13$. When the flight altitude increases from 20 km to 40 km, the shock extrapolation distance increases sharply from 1.98 mm to 32.11 mm, representing an increase of approximately 16-fold.

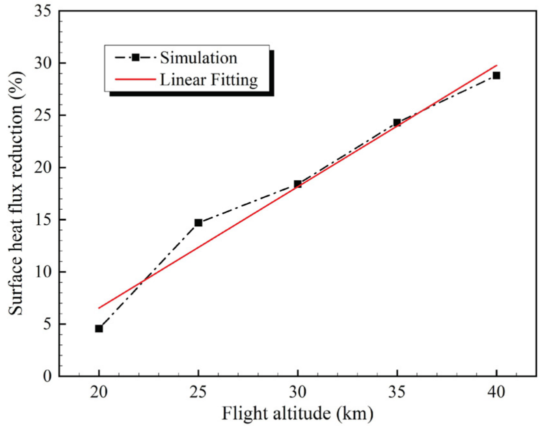

Fig. 17. Variation curve of surface heat flux reduction at Ma=15.

The reduction in surface heat flux increases linearly with increasing flight altitude, as shown in Fig. 17. The linear fitting relationship is expressed as follows:

$$y = kx + c, \tag{15}$$

where $k = 0.178$ and $c = 0.13$. When the flight altitude increases from 20 km to 40 km, the reduction in surface heat flux increases from 4.56 % to 28.81 %, representing an approximately 6-fold increase.

In summary, the flight altitude has no discernible effect on the variation patterns of the shock extrapolation distance and surface heat flux reduction as the Mach number increases. However, a decrease in the flight altitude leads to a significant decline in both the magnetic shock wave control efficacy and the thermal protection performance. The optimal Mach numbers for achieving magnetic shock wave control and thermal protection are 13 and 15, respectively. Notably, at Mach 13, the magnetic shock wave control efficacy exhibits an exponential dependence on the flight altitude, whereas at Mach 15, the magnetic thermal protection performance correlates linearly with the altitude variation. These findings highlight the altitude-dependent scaling laws that are critical for optimizing MHD control strategies in hypersonic flow regimes.

5. Results and discussion

A numerical simulation investigation of MHD flow control under mid-low altitude and hypersonic conditions was conducted in this study. The analysis revealed the mechanisms and scaling laws that govern the behavior of magnetically controlled shock waves and their thermal protection effects across different flight altitudes and freestream Mach numbers.

The key conclusions drawn are as follows:

1. Under mid-low altitude and hypersonic flight conditions, the methods and models used in this study have been validated as appropriate and effective in simulating the effects of MHD control.
2. The magnetically controlled shock standoff distance and the reduction in surface heat flux initially increase and then decrease as the Mach number increases, indicating the presence of an optimal parameter range. At a flight altitude of 40 km, the optimal Mach number range for MHD control is 13–17. Specifically, the optimal Mach number for shock wave control is 13, whereas the optimal thermal protection occurs at Mach 15. Under these conditions, the maximum reduction in surface heat flux can reach 28.81 %.
3. At Mach 13, the magnetically controlled shock extrapolation distance exhibits an approximate exponential dependence on the flight altitude, indicating rapid expansion of the MHD influence region with increasing altitude.
4. At Mach 15, the surface heat flux reduction demonstrates near-linear scaling with altitude, confirming the progressively enhanced thermal protection effectiveness at higher flight levels.

The present study supplements and refines the fundamental principles of hypersonic MHD control in low-to-medium altitude regimes, providing a theoretical foundation for MHD-based vehicle control across varying flight altitudes and offering valuable references for future flow control applications involving complex geometries. However, MHD-controlled shock waves and thermal protection systems are not only influenced by the Mach number and altitude but also critically depend on the magnetic field parameters, plasma distribution characteristics, and vehicle configurations. Therefore, subsequent research should focus on more comprehensive and in-depth investigations of these phenomena and their underlying mechanisms.

Declaration of competing interest

The authors declare that they have no known competing financial interests or personal relationships that could have appeared to influence the work reported in this paper.

CRediT authorship contribution statement

Yongchun Yan: Writing – original draft, Validation, Software, Methodology, Formal analysis, Data curation, Conceptualization. **Juan Ma:** Writing – review & editing, Conceptualization. **Mingsong Ding:** Writing – review & editing, Software, Methodology, Funding acquisition, Conceptualization. **Jianqiang Chen:** Writing – review & editing, Conceptualization.

Supplementary materials

Supplementary material associated with this article can be found, in the online version, at doi:10.1016/j.taml.2025.100617.

References

[1] Y. L, B. Zhang, Y. Li, et al., Adv. Mech. 47 (13) (2017).
[2] B. Zhang, T. Zhu, Y. Li, et al., Mech. Eng. 35 (2013) 02.
[3] Y. Li, Q. Wang, K. Luo, et al., Chin. J. Theor. Appl. Mech. 53 (2021) 09.
[4] K. Li, W. Liu, J. Natl. Univ. Def. 38 (2) (2016).
[5] T. Wang, B. Zhang, Y. Li, J. Propuls. Technol. 38 (11) (2017).
[6] X. Yao, W. Liu, J. Tan, Acta Phys. Sin. 67 (17) (2018).
[7] M. Ding, T. Jiang, Q. Liu, Acta Aeronaut. Astronaut. Sin. 40 (11) (2019).
[8] M. Ding, Q. Liu, T. Jiang, et al., Acta Aeronaut. Astronaut. Sin. (02) (2020).
[9] K. Luo, Q. Wang, Y. Li, et al., Chin. J. Theor. Appl. Mech. 53 (2021) 06.
[10] A. Cristofolini, C. Borghi, G. Neretti, in: 18th AIAA/3AF International Space Planes and Hypersonic Systems and Technologies Conference, 2012, pp. 2012–5804.
[11] A. Gulhan, B. Esser, U. Koch, F. Siebe, Spacecr. Rockets 46 (2009) 274.
[12] N. Bisek, in: 49th AIAA Aerospace Sciences Meeting including the New Horizons Forum and Aerospace Exposition, 2011, pp. 2011–2897.
[13] V. Bityurin, A. Bocharov, 42nd AIAA Plasmadynamics and Lasers Conference, 2011.
[14] K. Li, W. Liu, Acta Phys. Sin. 65 (2016) 06.
[15] M. Ding, Q. Liu, T. Jiang, et al., Acta Aeronaut. Astronaut. Sin. 42 (2021) 06.
[16] Z. Teng, Z. Zhou, Z. Zhang, et al., Aerodyn. Res. Exp. 02 (2024) 01.
[17] Z. Tian, National university of defense technology, 2008.
[18] H.R. Pletcher, C.J. Tannehill, D. Anderson, Computational Fluid Mechanics and Heat Transfer, Third Edition[M]. Taylor and Francis, 2012 -09-19.
[19] S. Macheret, M. Shneider, G. Candler, 42nd AIAA Aerospace Sciences Meeting and Exhibit, 2004 2004-1024.
[20] V. Bityurin, A. Bocharov, J. Lineberry, in: AIAA/CIRA 13th International Space Planes and Hypersonics Systems and Technologies Conference, 2005, pp. 2005–3225.
[21] G. Chen, J. Zhang, C. Li, Chin. J. Theor. Appl. Mech. 40 (2008) 06.
[22] K. Li, National university of defense technology, 2017.
[23] M. Ding, T. Jiang, W. Dong, et al., Acta Aeronaut. Astronaut. Sin. 38 (2017) 08.
[24] H. Huang, H. Huang, X. Zhang, et al., J. Propuls. Technol. 34 (2013) 05.